

MAGNETIC FIELD STRUCTURES AND TURBULENT COMPONENTS IN THE STAR-FORMING MOLECULAR CLOUDS OMC-2 AND OMC-3

FRÉDÉRIC POIDEVIN¹, PIERRE BASTIEN², AND BRENDA C. MATTHEWS³

¹ Universidade de São Paulo, Instituto de Astronomia, Geofísica e Ciências Atmosféricas, Rua do Matão 1226, Butantã, São Paulo, SP 05508-900, Brazil; Poidevin@astro.iag.usp.br

² Département de Physique and Observatoire du Mont-Mégantic, Université de Montréal, C.P. 6128, Succ. Centre-ville, Montréal, Québec H3C 3J7, Canada; Bastien@astro.umontreal.ca

³ Herzberg Institute of Astrophysics, National Research Council of Canada, Victoria, BC, Canada; brenda.matthews@nrc-cnrc.gc.ca

Received 2009 February 28; accepted 2010 March 25; published 2010 May 25

ABSTRACT

The SCUBA polarized 850 μm thermal emission data of the OMC-2 region in Orion A are added to and homogeneously reduced with data already available in the OMC-3 region. The data set shows that OMC-2 is a region generally less polarized than OMC-3. Where coincident, most of the 850 μm polarization pattern is similar to that measured in 350 μm polarization data. Only 850 μm polarimetry data have been obtained in and around MMS7, FIR1 and FIR2, and in the region south of FIR6. A realignment of the polarization vectors with the filament can be seen near FIR1 in the region south of OMC-3. An analysis shows that the energy injected by CO outflows and H₂ jets associated with OMC-2 and OMC-3 does not appear to alter the polarization patterns at a scale of the 14'' resolution beam. A second-order structure function analysis of the polarization position angles shows that OMC-2 is a more turbulent region than OMC-3. OMC-3 appears to be a clear case of a magnetically dominated region with respect to the turbulence. However, for OMC-2 it is not clear that this is the case. A more in-depth analysis of five regions displayed along OMC-2/3 indicates a decrease of the mean polarization degree and an increase of the turbulent angular dispersion from north to south. A statistical analysis suggests the presence of two depolarization regimes in our maps: one regime including the effects of the cores, the other one excluding it.

Key words: ISM: individual objects (OMC-2, OMC-3) – ISM: jets and outflows – magnetic fields – polarization – turbulence

Online-only material: color figures, machine-readable tables

1. INTRODUCTION

It is generally believed that magnetic fields play an important role in star formation but the evolution of their role from the scale of molecular clouds to that of young stellar objects is still not well understood. One of the best methods for their study is polarimetry of the continuum radiation emitted by aligned dust grains at far-infrared (FIR) to submillimeter (sub-mm) wavelengths (e.g., Dotson et al. 2000; Hildebrand et al. 1999; Matthews et al. 2009). Due to fast rotating mechanisms, elongated grains pervading the dense interstellar medium (ISM) should mostly have their longer axis preferentially oriented perpendicular to the local magnetic field. Recent advances on grain alignment theory can be found in reviews by Lazarian (2003, 2007).

The Orion “integral-shaped filament” (ISF) was mapped at 850 μm by Johnstone & Bally (1999). It contains the well-studied OMC-1 region behind the Orion nebula at ≈ 414 pc (see Menten et al. 2007), and the two filamentary structures OMC-2 and OMC-3 located $\approx 15'$ and $\approx 25'$ north of OMC-1, respectively. Sub-mm continuum and polarimetry observations in OMC-1 were intensively analyzed and discussed by Keene et al. (1982), Hildebrand et al. (1984), Aitken et al. (1997), Lis et al. (1998), Rao et al. (1998), Schleuning (1998), Vallée & Bastien (1999), Coppin et al. (2000), and Vallée & Fiege (2007). The counterparts to these studies in OMC-2 and more particularly in OMC-3 were discussed by Chini et al. (1997) with 1.3 mm dust emission observations in both regions, by Matthews & Wilson (2000) and Matthews et al. (2001) with 850 μm polarimetry in OMC-3, by Houde et al. (2004) with polarimetry at 350 μm in both filaments, and more recently by

Matthews et al. (2005) with 1.3 mm high resolution observations in the MMS6 protostellar core in OMC-3.

The 850 μm polarization pattern of OMC-3 measured with the Submillimeter Common User Bolometric Array (SCUBA) and studied by Matthews et al. (2001) shows that a helical magnetic field (see Fiege & Pudritz 2000) could thread the filament. The change in orientation between the polarization data and the filamentary axis to the south of OMC-3 could be accounted for by either a bend of the filament or the presence of a second filament, oriented roughly orthogonal to the primary ISF. If the latter interpretation is correct, then polarization vectors realigning with the filamentary axis are expected south of OMC-3. If the filament continues to bend, then any orientation of vectors to the filament axis is possible.

Our initial motivation for this project was to measure the 850 μm polarization pattern of OMC-2 with the aim to better understand the structure of the magnetic field south of OMC-3. Then, with the availability of 350 μm polarization data by Houde et al. (2004) and estimates of the orientation of the magnetic field relative to the line of sight (LOS) at several places along the filament, a global comparison with the 850 μm polarization vectors observed in both regions can be made. Abundances of several molecular species and clumping were also observed in these regions (e.g., Batrla et al. 1983; Castets & Langer 1995; Chini et al. 1997) suggesting an evolutionary effect from north to south along OMC-3/2. In contrast, Takahashi et al. (2008) show that some intermediate-mass (IM) star-forming objects in OMC-3 can be at a more evolved stage than some less active IM star-forming objects in OMC-2. Observations of H₂ jets (e.g., Stanke et al. 2002; Park & Choi 2006) and of molecular outflows (e.g., Williams et al. 2003) allowed the

detection of some progenitors along the chain of active cores embedded in the filament with relatively good certainty. Thus, we can compare their respective orientations on the plane of sky (POS) with the direction of polarization vectors in order to statistically study the impact of outflow and jet activity on the region. The distribution of the offsets in position angles (P.A.s) obtained in this way can help to test the detectability of turbulence in the framework of our observations. In addition, a coherent structure function analysis method was recently put forth by Hildebrand et al. (2009). Combined with other analysis tools, this promising approach should help to make fruitful comparisons with available and future models. As a consequence, we can use this method along the OMC-2 and OMC-3 filamentary molecular clouds and compare it with steady-state and turbulent magnetic field models. All in all, these approaches should help us to better understand the impact of magnetic fields with respect to turbulence and gravity in star-forming processes and cloud evolution.

In this work, we present 850 μm SCUBA polarization data of OMC-2. Observations and data reduction techniques are presented and discussed in Section 2. Results are shown and analyzed in Section 3. A discussion and comparisons with models follow in Section 4.

2. OBSERVATIONS AND DATA REDUCTION

The observations were carried out on the summit of Mauna Kea in Hawaii, from 2004 September 14 to 20 and on 2005 January 16 with the SCUPOL polarimeter installed in front of the SCUBA detector (Holland et al. 1998) mounted on the James Clerk Maxwell Telescope (JCMT). The nights were relatively stable with τ (225 GHz) ranging from 0.04 to 0.07 during the periods of observations. The polarimeter and general reduction techniques are described by Greaves et al. (2003).

The SCUBA User Reduction Facility (SURF; see Jenness & Lightfoot 1998) and KAPPA reduction packages were used for flatfielding, extinction correction, instrumental polarization removal, sky noise removal, despiking, removal of bad pixels, and rebinning of the images. The Starlink software packages POLPACK and CURSA were also used for combining, binning, and filtering the Stokes parameters of the images to finally extract the polarized source signal.

After extinction correction, noisy bolometers were identified and removed from the data sets. At 850 μm , effects due to sky variations were subtracted by using bolometers devoid of significant target flux. We used between one and four bolometers to determine sky variability, using the existing 850 μm map of total intensity of the ISF produced by Johnstone & Bally (1999) to help select empty bolometers. Bolometers that were significantly negative were avoided since they can greatly affect the interpretation of the final map by possibly injecting polarized emission in the bolometers probing the source (see Appendix B of Matthews et al. 2001 for more details). The mean flux removed by sky subtraction was added back into the maps since the flux from sky emission was not necessarily always close enough to zero.

During observations, the atmospheric variability was canceled by chopping. The pointing center, the chop P.A., the distance to the center of the chop position, and the number of observations for each of the seven different SCUBA fields required to map the OMC-2 filament and the southernmost portion of OMC-3 are shown in Table 1.

After removal of the instrumental polarization in each bolometer, the Stokes parameters Q , U , and I for each set of

Table 1
Observational Parameters for Jiggle Mapping Polarimetry in OMC-2

Pointing Center R.A. (J2000)	Pointing Center Decl. (J2000)	Chop Position East from North ($^\circ$)	Angle Distance ($''$)	Number of Observations
05 35 22.2	-05 06 40.1	112	180	9
05 35 25.0	-05 07 49.3	90	150	12
05 35 26.8	-05 09 13.5	90	150	12
05 35 25.0	-05 10 37.4	90	150	18
05 35 24.9	-05 12 07.3	90	150	15
05 35 21.9	-05 13 19.1	90	150	12
05 35 18.8	-05 14 54.9	90	150	12

data were combined to produce a final cube of data where Q_{tot} and U_{tot} are the two components of linearly polarized light and I_{tot} is the total intensity associated with each $6''.18$ pixel of the map. The polarization percentage, p , and the polarization P.A., θ , are, respectively, defined according to the usual relations

$$p = \frac{\sqrt{Q^2 + U^2}}{I}, \quad (1)$$

$$\theta = \frac{1}{2} \arctan\left(\frac{U}{Q}\right). \quad (2)$$

The uncertainties on p and θ are, respectively, given by

$$\sigma_p = \frac{\sqrt{dQ^2 Q^2 + dU^2 U^2}}{p}, \quad (3)$$

$$\sigma_\theta = 28.6 \left(\frac{p}{\sigma_p}\right)^{-1}, \quad (4)$$

where $\frac{p}{\sigma_p}$ is the signal-to-noise ratio (S/N) in p . The polarization defined in Equation (1) is overestimated and needs to be debiased using the relation

$$p_{\text{db}} = \sqrt{p^2 - \sigma_p^2}. \quad (5)$$

In what follows we refer to p_{db} and we call it p .

OMC-2 data were combined with SCUBA data of OMC-3 (see Matthews & Wilson 2000; Matthews et al. 2001) retrieved from the JCMT data archive. Since the data reduction does not provide an absolute sensitivity to the polarization intensity, appropriate values of the flux calibration factors (FCFs) were defined by comparing the intensity flux levels of the OMC-2 and OMC-3 intensity maps with the ISF continuum map of Johnstone & Bally (1999) and the OMC-2/3 map of Di Francesco et al. (2008). This ensures a reasonable similarity between the OMC-3 and OMC-2 data sets. The values of the FCFs employed were 484 Jy beam $^{-1}$ V $^{-1}$ in OMC-3 and 690 Jy beam $^{-1}$ V $^{-1}$ in OMC-2.

Overestimation of the S/N due to oversampling in the pixel scale was minimized during the reduction process by sampling to a larger grid than that used by Matthews et al. (2001). This means that our reduction is not exactly comparable to the earlier publication. Similarly, our reduction is not identical to that of Matthews et al. (2009; the SCUPOL Legacy Catalogue). Despite these differences in sampling, the results are generally consistent with one another.

The data for the 11 fields were reduced homogeneously and combined to produce a preliminary 850 μm polarization map covering both regions. In order to study the variations in the polarization patterns, this preliminary map was binned

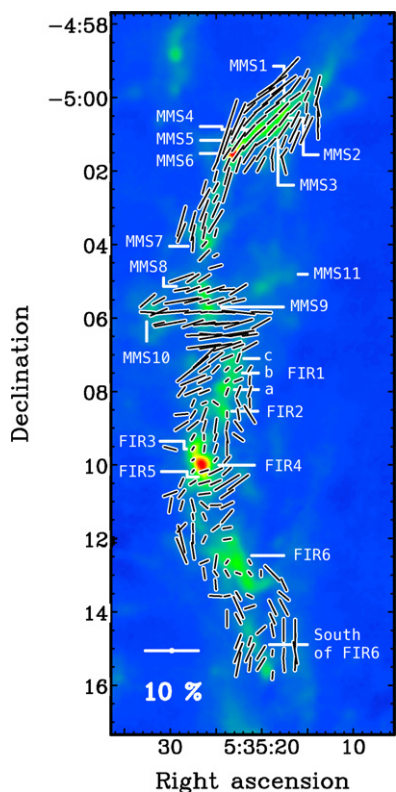


Figure 1. 850 μm map and polarimetry of the OMC-3 and OMC-2 regions obtained with SCUBA at the JCMT. The vector length denotes polarization percentage and the position angle denotes the E -vector orientation. The vectors have a polarization percentage and uncertainty such that $p/\sigma_p > 3$. Coordinates are J2000.0.

(A color version of this figure is available in the online journal.)

by factors of 1, 2, 3, 4, and 5 pixels, and each one of these maps was filtered with the following criteria $I_{\text{tot}} > 0$ and either $\sigma_p < 0.75\%$ or $\sigma_p < 1.0\%$. The 10 maps produced by these various combinations were compared with each other and we decided that the map binned to $\approx 18''.6$ (or $\approx 1.3 \times 14''$ beam resolution) improves p/σ_p and hence σ_θ sufficiently. This rebinning improves S/N by a factor of 3 over the unbinned $6''.18$ sampled data. The filtering criterion $\sigma_p < 0.75\%$ was then chosen because it avoids polarization artefacts in low emissivity regions due to binning effects.

3. RESULTS

The final 850 μm polarization map of OMC-2/OMC-3 is shown in Figure 1. We present detailed maps of four subregions of OMC-2 in Figure 2. We follow the same notation as Chini et al. (1997) in their figure to identify the cold condensations encountered along the filaments; they are also identified in our Figure 1. The vectors shown in the figures have $p/\sigma_p > 3$.

3.1. Degree of Polarization and Distribution of Polarization Position Angles

The polarization data along OMC-2 and OMC-3 are reported in Table 2 and Table 3, respectively. P.A.s are counted positively east of north. The results of a basic statistical analysis on several subsets of the sample are shown in Table 4 where mean P.A.s, $\langle \text{P.A.}_{\text{fila}} \rangle$, of the corresponding sections of the filaments are displayed. These mean orientations within the filament were estimated by eye with the help of contour maps.

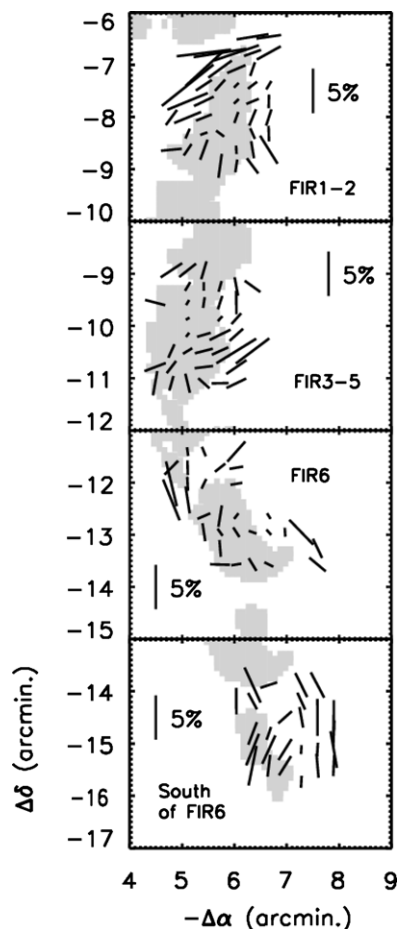


Figure 2. Zoom on the four regions located along OMC-2 and displayed in Table 4. All the data shown here have a S/N such that $p/\sigma_p > 3$. A background intensity map ($I(850 \mu\text{m}) \geq 0.5 \text{ Jy pixel}^{-1}$, where pixels are $3'' \times 3''$ in size) is displayed and shows the location of the filament. The reference position is R.A. = $5^{\text{h}}35^{\text{m}}23^{\text{s}}.5$, decl. = $-5^{\circ}01'32''.2$ (J2000.0); see Figure 1 for comparisons.

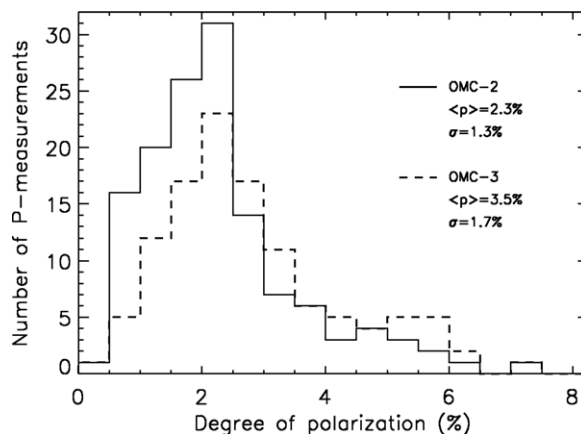


Figure 3. Histogram of 850 μm degree of polarization through OMC-3 and OMC-2 based on data shown in Figure 1.

The histograms of the OMC-2 and OMC-3 polarization percentages data sets are shown in Figure 3. The mean polarization of the combination of the two data sets is $\langle p \rangle = 2.8\%$ with a dispersion of 1.6%. Within the uncertainties, no polarization vector greater than 12% can be seen in the distribution. Vectors within OMC-3 show a mean polarization percentage of $\langle p \rangle = 3.5\%$, slightly higher than the mean polarization percentage of $\langle p \rangle = 2.3\%$ found within OMC-2.

Table 2
850 μm Polarization Data Through OMC-2

ID ^a	R.A. (J2000) (^h ^m ^s)	Decl. (J2000) ([°] ['] ^{''})	p (%)	σ_p (%)	θ^b ([°])	σ_θ ([°])	Flux (Jy/18''6 beam)
1	05 35 18.89	-05 15 43.9	1.34	0.39	-3.1	8.2	1.5
2	05 35 22.61	-05 15 25.4	4.54	0.61	-11.5	3.8	0.9
3	05 35 21.37	-05 15 25.4	2.46	0.50	-6.8	5.7	1.1
4	05 35 20.13	-05 15 25.4	2.54	0.24	-32.1	2.8	2.3
5	05 35 17.65	-05 15 25.4	2.73	0.51	4.9	5.2	1.1
6	05 35 16.41	-05 15 25.4	2.33	0.58	-2.7	6.3	1.0
7	05 35 22.61	-05 15 06.9	3.83	0.46	-22.0	3.4	1.3
8	05 35 21.37	-05 15 06.9	3.50	0.35	-24.7	2.9	1.6
9	05 35 20.13	-05 15 06.9	2.78	0.29	-31.8	3.0	1.9
10	05 35 18.89	-05 15 06.9	0.99	0.32	-3.9	9.0	1.5
11	05 35 17.65	-05 15 06.9	1.52	0.42	-3.3	7.0	1.2
12	05 35 16.41	-05 15 06.9	4.18	0.45	9.7	2.9	1.2
13	05 35 22.61	-05 14 48.3	2.70	0.48	-21.0	5.0	1.5
14	05 35 21.37	-05 14 48.3	1.52	0.27	-18.7	5.0	2.1
15	05 35 16.41	-05 14 48.3	2.95	0.56	-2.4	5.3	0.9
16	05 35 20.13	-05 14 29.8	2.04	0.40	-48.2	6.0	1.2
17	05 35 18.89	-05 14 29.8	2.34	0.58	10.0	6.8	1.0
18	05 35 17.65	-05 14 29.8	4.16	0.68	0.2	4.4	1.0
19	05 35 16.41	-05 14 29.8	3.86	0.65	-0.3	5.3	0.7
20	05 35 23.86	-05 14 11.2	2.98	0.59	0.1	5.8	1.0
21	05 35 22.61	-05 14 11.2	2.08	0.39	28.4	5.4	1.5
22	05 35 18.89	-05 14 11.2	2.07	0.45	24.7	6.1	1.2
23	05 35 22.61	-05 13 52.7	4.33	0.63	24.6	4.1	0.9
24	05 35 21.37	-05 13 52.7	1.97	0.48	-71.9	6.8	1.1
25	05 35 18.89	-05 13 52.7	3.01	0.56	26.2	5.1	0.9
26	05 35 17.65	-05 13 52.7	3.21	0.59	27.9	5.2	0.9
27	05 35 25.10	-05 13 34.2	2.22	0.52	88.3	6.9	0.8
28	05 35 23.86	-05 13 34.2	1.10	0.36	-80.8	8.5	1.3
29	05 35 22.61	-05 13 34.2	1.66	0.33	31.0	5.8	1.7
30	05 35 21.37	-05 13 34.2	1.10	0.31	64.3	8.1	1.9
31	05 35 17.65	-05 13 34.2	2.39	0.71	50.0	8.0	0.9
32	05 35 25.10	-05 13 15.6	1.87	0.33	4.7	5.1	1.2
33	05 35 17.65	-05 13 15.6	2.37	0.71	25.4	8.3	0.9
34	05 35 26.34	-05 12 57.1	2.04	0.52	8.6	7.4	0.8
35	05 35 25.10	-05 12 57.1	0.96	0.27	35.6	7.6	1.5
36	05 35 23.86	-05 12 57.1	1.27	0.15	32.8	3.6	2.4
37	05 35 22.61	-05 12 57.1	0.91	0.11	70.6	3.4	3.6
38	05 35 21.37	-05 12 57.1	0.78	0.14	42.2	5.0	3.0
39	05 35 20.13	-05 12 57.1	0.99	0.28	3.9	8.0	1.6
40	05 35 18.89	-05 12 57.1	3.87	0.54	44.0	3.9	1.0
41	05 35 26.34	-05 12 38.5	1.56	0.42	-66.8	7.3	1.2
42	05 35 25.10	-05 12 38.5	2.42	0.21	-9.1	2.5	2.3
43	05 35 23.86	-05 12 38.5	0.78	0.13	-38.0	5.0	3.5
44	05 35 21.37	-05 12 38.5	0.73	0.24	31.9	9.2	1.9
45	05 35 28.82	-05 12 20.0	4.94	0.62	22.1	3.6	1.0
46	05 35 27.58	-05 12 20.0	3.05	0.53	8.7	4.6	1.1
47	05 35 28.82	-05 12 01.5	5.17	0.72	13.4	4.1	1.0
48	05 35 27.58	-05 12 01.5	1.57	0.43	2.8	7.6	1.1
49	05 35 26.34	-05 12 01.5	1.22	0.38	-26.4	8.5	1.4
50	05 35 23.86	-05 12 01.5	1.34	0.22	-80.5	4.9	2.4
51	05 35 28.82	-05 11 42.9	2.17	0.59	-44.4	7.2	0.9
52	05 35 27.58	-05 11 42.9	1.61	0.23	1.8	5.3	1.5
53	05 35 25.10	-05 11 42.9	1.47	0.31	-51.7	6.2	1.3
54	05 35 23.86	-05 11 42.9	1.54	0.35	-80.4	6.0	1.5
55	05 35 27.58	-05 11 24.4	0.97	0.26	8.0	7.7	1.7
56	05 35 26.34	-05 11 24.4	1.14	0.36	22.2	8.7	1.2
57	05 35 23.86	-05 11 24.4	3.01	0.45	-41.6	4.3	1.0
58	05 35 30.06	-05 11 05.8	2.76	0.74	-9.8	7.7	0.9
59	05 35 28.82	-05 11 05.8	1.68	0.36	-15.5	6.1	1.4
60	05 35 27.58	-05 11 05.8	2.19	0.33	13.2	4.2	1.6
61	05 35 26.34	-05 11 05.8	1.68	0.33	48.0	6.5	1.4
62	05 35 25.10	-05 11 05.8	1.92	0.50	-88.7	7.4	0.9
63	05 35 23.86	-05 11 05.8	2.46	0.50	-64.5	5.7	0.8
64	05 35 30.06	-05 10 47.3	2.55	0.68	-69.2	7.4	1.0
65	05 35 28.82	-05 10 47.3	1.72	0.41	-37.6	6.6	1.7

Table 2
(Continued)

ID ^a	R.A. (J2000) (^h ^m ^s)	Decl. (J2000) ([°] ['] ^{''})	p (%)	σ_p (%)	θ^b ([°])	σ_θ ([°])	Flux (Jy/18''6 beam)
66	05 35 26.34	-05 10 47.3	2.08	0.24	-82.9	3.7	2.5
67	05 35 23.86	-05 10 47.3	2.74	0.61	-55.5	6.4	0.9
68	05 35 28.82	-05 10 28.8	1.64	0.26	-24.1	4.5	2.4
69	05 35 27.58	-05 10 28.8	1.20	0.17	-58.8	3.9	3.9
70	05 35 26.34	-05 10 28.8	2.06	0.13	-75.5	1.9	4.8
71	05 35 25.10	-05 10 28.8	2.02	0.23	-65.5	3.2	2.6
72	05 35 23.86	-05 10 28.8	5.26	0.43	-58.3	2.3	1.2
73	05 35 22.61	-05 10 28.8	4.69	0.45	-52.9	2.8	1.2
74	05 35 27.58	-05 10 10.2	0.56	0.13	-37.8	6.5	5.7
75	05 35 26.34	-05 10 10.2	1.58	0.11	-73.6	1.9	7.7
76	05 35 25.10	-05 10 10.2	2.62	0.20	-63.8	2.2	2.9
77	05 35 23.86	-05 10 10.2	2.02	0.32	-48.1	4.4	1.8
78	05 35 27.58	-05 09 51.7	0.45	0.11	-59.2	6.8	7.6
79	05 35 25.10	-05 09 51.7	0.74	0.24	-42.6	9.6	2.4
80	05 35 23.86	-05 09 51.7	1.62	0.39	-41.9	6.8	1.5
81	05 35 30.06	-05 09 33.1	2.32	0.55	75.3	6.6	1.2
82	05 35 27.58	-05 09 33.1	0.65	0.09	-31.3	4.0	5.7
83	05 35 26.34	-05 09 33.1	1.20	0.14	-8.7	3.3	3.4
84	05 35 25.10	-05 09 33.1	1.57	0.23	-18.2	4.1	1.9
85	05 35 23.86	-05 09 33.1	2.63	0.33	0.5	3.5	1.4
86	05 35 27.58	-05 09 14.6	1.12	0.14	-30.7	3.6	3.7
87	05 35 26.34	-05 09 14.6	0.96	0.16	-0.4	4.8	2.9
88	05 35 25.10	-05 09 14.6	1.23	0.22	-15.5	5.0	2.0
89	05 35 23.86	-05 09 14.6	2.09	0.34	10.4	4.6	1.4
90	05 35 22.61	-05 09 14.6	2.15	0.60	54.2	7.7	0.9
91	05 35 28.82	-05 08 56.1	2.88	0.61	-56.5	6.0	1.2
92	05 35 27.58	-05 08 56.1	2.40	0.36	-51.6	4.1	1.8
93	05 35 26.34	-05 08 56.1	2.08	0.30	-16.3	4.2	1.7
94	05 35 25.10	-05 08 56.1	2.71	0.22	-7.8	2.4	2.1
95	05 35 23.86	-05 08 56.1	1.44	0.32	-8.5	6.0	1.8
96	05 35 22.61	-05 08 56.1	2.11	0.60	36.9	7.9	1.1
97	05 35 28.82	-05 08 37.5	2.33	0.56	-84.6	7.0	0.8
98	05 35 27.58	-05 08 37.5	1.54	0.38	-33.8	6.6	1.5
99	05 35 26.34	-05 08 37.5	2.39	0.30	-19.9	3.6	2.1
100	05 35 23.86	-05 08 37.5	0.94	0.25	2.9	7.5	2.6
101	05 35 22.61	-05 08 37.5	1.93	0.38	9.2	6.1	1.5
102	05 35 21.37	-05 08 37.5	3.70	0.73	31.9	5.6	1.1
103	05 35 27.58	-05 08 19.0	1.18	0.37	-23.9	8.6	1.6
104	05 35 26.34	-05 08 19.0	0.84	0.25	-70.1	8.2	2.3
105	05 35 25.10	-05 08 19.0	1.10	0.20	53.2	4.6	2.6
106	05 35 22.61	-05 08 19.0	1.29	0.31	24.0	6.7	1.8
107	05 35 21.37	-05 08 19.0	1.73	0.54	1.7	8.9	1.2
108	05 35 28.82	-05 08 00.4	2.09	0.56	-36.5	7.3	1.0
109	05 35 27.58	-05 08 00.4	3.25	0.44	-67.6	3.9	1.4
110	05 35 26.34	-05 08 00.4	1.91	0.36	-68.2	5.3	1.6
111	05 35 23.86	-05 08 00.4	1.30	0.17	-20.1	3.8	3.0
112	05 35 22.61	-05 08 00.4	1.97	0.26	-22.3	3.7	2.1
113	05 35 21.37	-05 08 00.4	1.92	0.51	-18.0	7.2	1.1
114	05 35 27.58	-05 07 41.9	4.90	0.59	-67.5	3.5	1.1
115	05 35 26.34	-05 07 41.9	2.44	0.48	-64.6	5.4	1.2
116	05 35 23.86	-05 07 41.9	0.73	0.16	-45.0	6.7	3.2
117	05 35 22.61	-05 07 41.9	1.50	0.21	-67.8	4.0	2.1
118	05 35 21.37	-05 07 41.9	1.52	0.33	-1.7	6.2	1.2
119	05 35 27.58	-05 07 23.4	7.43	0.59	-51.3	2.3	1.0
120	05 35 26.34	-05 07 23.4	2.14	0.37	-56.3	4.8	1.2
121	05 35 25.10	-05 07 23.4	1.68	0.29	-41.9	4.6	1.5
122	05 35 23.86	-05 07 23.4	0.73	0.17	-46.3	6.0	2.7
123	05 35 22.61	-05 07 23.4	1.27	0.21	-52.5	4.8	2.3
124	05 35 21.37	-05 07 23.4	1.09	0.31	-31.2	7.8	1.4
125	05 35 26.34	-05 07 04.8	5.58	0.52	-47.3	2.5	0.8
126	05 35 25.10	-05 07 04.8	3.25	0.36	-53.9	3.0	1.3
127	05 35 23.86	-05 07 04.8	2.22	0.21	-66.9	2.7	2.3
128	05 35 22.61	-05 07 04.8	1.62	0.24	-18.4	4.2	2.1
129	05 35 26.34	-05 06 46.3	6.14	0.56	-83.1	2.7	0.6
130	05 35 25.10	-05 06 46.3	5.99	0.55	-81.0	2.6	0.7

Table 2
(Continued)

ID ^a	R.A. (J2000) (h m s)	Decl. (J2000) (° ' ")	p (%)	σ_p (%)	θ^b (°)	σ_θ (°)	Flux (Jy/18"6 beam)
131	05 35 23.86	-05 06 46.3	5.36	0.37	-71.3	1.9	1.2
132	05 35 22.61	-05 06 46.3	2.02	0.28	-70.4	3.8	1.8
133	05 35 21.37	-05 06 46.3	3.06	0.50	-61.0	4.9	1.1
134	05 35 22.61	-05 06 27.7	3.61	0.34	-80.8	2.5	1.3
135	05 35 21.37	-05 06 27.7	2.77	0.48	-81.7	4.5	1.1

Notes.

^a All the data shown here have a polarization level and uncertainty such that $p/\sigma_p > 3$.

^b P.A. of E -vector in degrees east from north.

(This table is also available in a machine-readable form in the online journal.)

Table 3
850 μm Polarization data Through OMC-3

ID ^a	R.A. (J2000) (h m s)	Decl. (J2000) (° ' ")	p (%)	σ_p (%)	θ^b (°)	σ_θ (°)	Flux (Jy/18"6 beam)
1	05 35 26.34	-05 06 27.7	6.54	0.44	-88.1	1.9	0.8
2	05 35 25.10	-05 06 27.7	5.98	0.65	84.7	3.2	0.5
3	05 35 23.86	-05 06 27.7	10.29	0.68	-81.4	2.1	0.5
4	05 35 31.30	-05 06 09.2	1.97	0.59	-76.8	7.6	0.7
5	05 35 30.06	-05 06 09.2	5.77	0.56	-79.2	2.7	0.6
6	05 35 27.58	-05 06 09.2	4.06	0.41	-71.3	2.9	1.0
7	05 35 26.34	-05 06 09.2	3.93	0.25	-81.8	1.9	1.5
8	05 35 25.10	-05 06 09.2	5.02	0.37	-86.9	2.1	1.0
9	05 35 23.86	-05 06 09.2	4.33	0.44	-84.2	3.1	0.7
10	05 35 22.61	-05 06 09.2	5.42	0.55	-72.9	3.0	0.7

Notes.

^a All the data shown here have a polarization level and uncertainty such that $p/e_p > 3$.

^b P.A. of E -vector in degrees east from north.

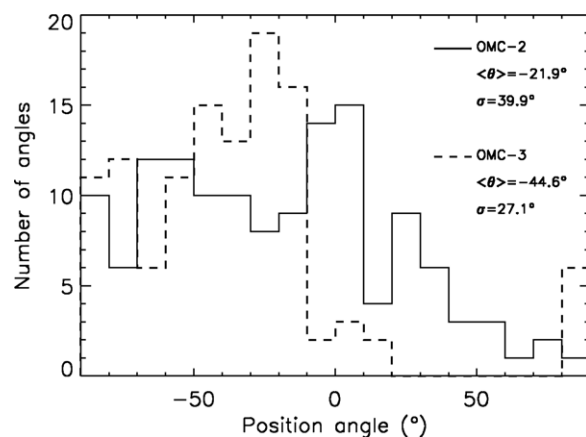
(This table is available in its entirety in a machine-readable form in the online journal. A portion is shown here for guidance regarding its form and content.)

The histograms of the P.A. distributions in OMC-2 and OMC-3 are shown in Figure 4. The combination of the distributions peaks around a P.A. of $\approx -35^\circ$ with a dispersion $\sigma_p \approx 36^\circ$. The OMC-3 data peaks around a P.A. of $\approx -45^\circ$ while the OMC-2 data peaks around a P.A. of $\approx -22^\circ$. The distribution of vectors within OMC-3 has a smaller dispersion, $\sigma_p \approx 27^\circ$, than the one within OMC-2 where $\sigma_p \approx 40^\circ$, in agreement with the more ordered polarization pattern observed in this region.

Figure 5 compares the 850 μm data with the 350 μm data of Houde et al. (2004). Only 850 μm data have been obtained in and around MMS7, FIR1, and FIR2, and in the region south of FIR6, while data at both wavelengths are available in other regions. The similarity between the polarization patterns can clearly be seen in most of the common areas where vectors at both wavelengths are detected. The same scale is used to plot the vectors; we also see that the polarization percentage is generally higher at 850 μm than at 350 μm . We now discuss OMC-2 regions as designated on Figure 1 more specifically.

3.1.1. FIR1 and 2

Houde et al. (2004) only show polarization data southward of FIR2. The data of Figures 1 and 2 contain the first sub-mm data polarimetry in this region. Polarization is detected toward FIR1 and FIR2 and along both sides of the filament. Depolarization is clearly visible from low to high column density in the direction of the densest regions. The filament is oriented at an angle of

**Figure 4.** Histogram of 850 μm polarization position angles through OMC-3 and OMC-2 based on data shown in Figure 1.

$\approx -17^\circ$. The mean P.A. of vectors covering FIR1 and FIR2 is -41.5° with a large dispersion of 35.6° . This mean P.A. is offset by $\approx 25^\circ$ with respect to the mean orientation of the filament in this region. Our vectors located in the region south of FIR2 show a polarization pattern consistent with the orientation of the 350 μm vectors shown in Figure 2 of Houde et al. (2004).

More generally, we point out that vectors located around and to the north of FIR1, although shifted by about 30° with the mean orientation of the filament in this region, have approximately the same orientation as vectors in the southern part of OMC-3. We also note that the high angular dispersion $s(\theta) = 35.6^\circ$ of the data set covering FIR1 and FIR2 implies a fast variation in P.A.s in a region having a spatial scale comparable in size with the region formed by MMS1 to MMS6 where the dispersion is approximately half of this value. Finally, the mean degree of polarization covering FIR1 and FIR2 is 2.5% with a dispersion of 1.6%.

3.1.2. FIR3, 4, and 5

The polarization pattern is consistent with that found by Houde et al. (2004) at 350 μm . The vectors north of FIR3 have P.A. $\approx 0^\circ$ while a clear rotation of $\approx 90^\circ$ can be seen when moving south of FIR5. This trend gives a mean P.A. of -47° over the region and a dispersion of $\approx 35^\circ$. The filament is oriented at an angle of $\approx -10^\circ$ on the POS. The mean level of polarization $\langle p \rangle = 2.0\%$ is the second lowest of the several subsets of data shown in Table 4 and the dispersion of the subset is 1.0%.

3.1.3. FIR6

Few detections are found in the densest emitting regions and the mean P.A. of 26.2° may indicate a mean alignment of the vectors with the filament which is oriented at $\approx 30^\circ$. Figure 5 shows that the 850 μm vectors are however generally inconsistent with the polarization pattern at 350 μm (Houde et al. 2004). Moreover, degrees of polarization measured at 850 μm appear to be about two to three times smaller than those measured at 350 μm . As mentioned above, our mean P.A. in the region is 26.2° with a dispersion of 44.5° while, based on average Stokes parameters, Houde et al. (2004) found a mean P.A. of $\approx -65^\circ \pm 6^\circ$. The reason for this difference is not obvious. The lower polarization percentage values are more prone to P.A. errors, for instance due to chopping onto polarized emission. There is no easy way to check this though. Finally, at 850 μm ,

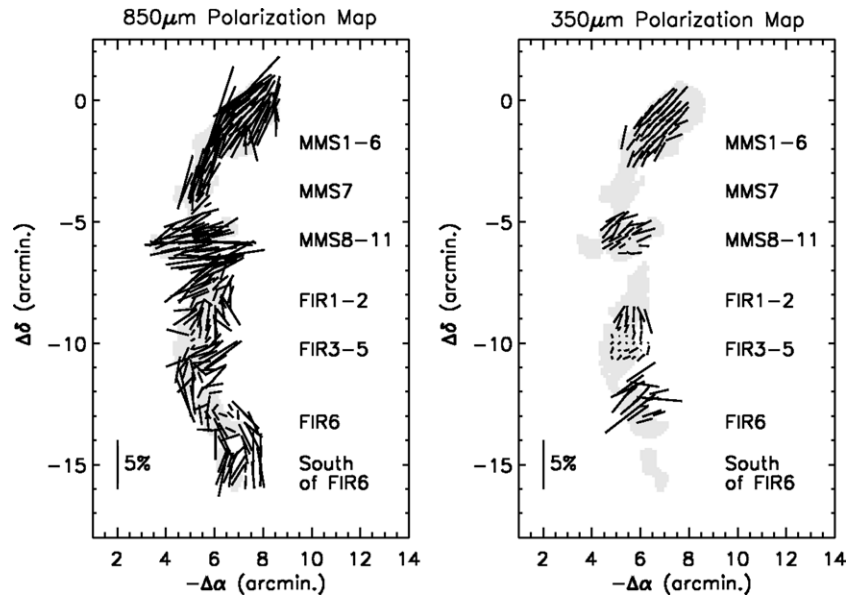


Figure 5. Left: 850 μm polarization map from this work. Right: 350 μm data from Houde et al. (2004). All the data shown here have an S/N such that $p/\sigma_p > 3$. Each set of data is drawn with the same scale for comparison. A background intensity map ($I(850 \mu\text{m}) \geq 0.5 \text{ Jy pixel}^{-1}$, where pixels are $3'' \times 3''$ in size) is displayed and shows the location of the filament. The reference position is R.A. = $5^{\text{h}}35^{\text{m}}48^{\text{s}}$, decl. = $-5^{\circ}00'0''$ (J2000.0).

Table 4
Mean Polarization Percentages and Position Angles Along OMC-3 and OMC-2

Region (See Figure 1)	Vectors ID (See Tables 2 and 3)	Number of Vectors	$\langle p \rangle$ (%)	$s(p)$ (%)	$\langle \theta \rangle$ ($^{\circ}$)	$s(\theta)$ ($^{\circ}$)	$\langle F \rangle$ (Jy/18''.6 beam)	$s(F)$ (Jy/18''.6 beam)	$\langle \text{P.A.}_{\text{fila}} \rangle$ ($^{\circ}$)
OMC2/OMC3	...	251	2.8	1.6	-34.6	35.6	1.6	1.0	...
OMC3	...	114	3.5	1.7	-44.6	27.1	1.3	0.9	...
OMC2	1:135	135	2.3	1.3	-21.9	39.9	1.7	1.2	...
MMS1 to MMS6	...	62	3.4	1.8	-30.3	17.0	1.6	1.0	-40
MMS7	...	17	2.9	1.3	-27.3	18.6	1.0	0.4	-18
MMS8, 9, and 10	...	37	3.8	1.8	-76.7	11.9	1.0	0.5	23 or 113 ^a
FIR1 and 2	94:135	42	2.5	1.6	-41.5	35.6	1.6	0.6	-17
FIR3, 4, and 5	58:93	36	2.0	1.0	-47.0	34.9	2.4	1.8	-10
FIR6	27:57	31	1.9	1.1	26.2	44.5	1.6	0.7	30
South of FIR6	1:26	26	2.8	1.0	-5.7	24.1	1.2	0.4	21

Note. ^a See discussion in Section 3.1.5.

the mean degree of polarization of 1.9% is the lowest of all the subsets of data shown in Table 4 with a dispersion of 1.1%.

3.1.4. South of FIR6

These measurements are the first to probe aligned grains with sub-mm polarimetry in this region. The vectors are relatively well aligned around a mean P.A. of $-5^{\circ}7'$ with a dispersion of $24^{\circ}1'$ and are offset by $\approx 27^{\circ}$ from the ridge orientation. The mean degree of polarization is 2.8% with a dispersion of 1.0%.

3.1.5. OMC-3

The 850 μm data shown by Matthews et al. (2001) were already compared with 350 μm data by Houde et al. (2004); therefore, we will not discuss this region in detail here. Table 4 contains the mean and dispersion of polarization percentages of several regions of OMC-3. We point out, however, that while MMS10 is located at approximately the same declination as MMS8 and 9 but at a position $\approx 1'30''$ to the east, another dense condensation with no apparent star-forming core can be seen to the west of MMS8 at approximately the same distance. In Figure 1, we have identified this faint condensation by ‘‘MMS11.’’

With the data in OMC-2, we now see that a realignment of the polarization pattern with the filamentary structure is effective just to the south of OMC-3, near FIR1. Data are not available in MMS11 but this realignment suggests that there is effectively a second filament crossing the region located from MMS10 to MMS11. We point out, however, that such a realignment does not reject the possibility of a double bend of the filament with one bend located to the north of the region MMS8 or around the region MMS10, and with the other one located to the south of the region MMS11 (see Matthews et al. 2001 and Fiege & Pudritz 2000 for more details).

3.2. Polarization Hole

In studies of polarized radiation emitted by aligned dust grains, it is usual to show the distribution of polarization as a function of intensity. Many of these distributions show a depolarization effect where p decreases when I increases. Such an effect was shown by Matthews et al. (2001) in OMC-3, and Figure 6 shows that it can also be seen in OMC-2. The dashed lines are χ^2 power-law fits of the form $p = AI^{\nu}$ to the OMC-2 (left) and OMC-3 (right) data sets.

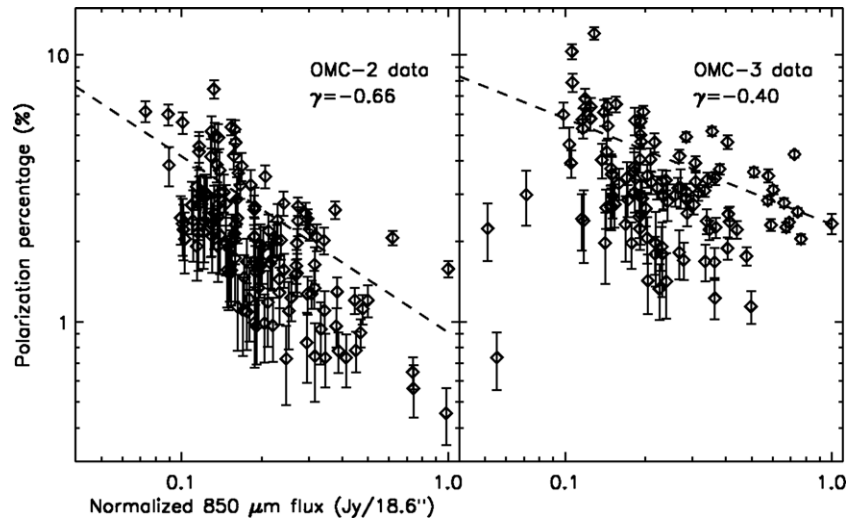


Figure 6. Percentage of polarization vs. $850 \mu\text{m}$ normalized continuum flux of the polarization data set in OMC-3 and OMC-2 shown in Figure 1. All the data shown here have a polarization percentage and uncertainty such that $p/\sigma_p > 3$ (see Figure 1). The dashed lines are χ^2 power-law fits of the form $p = A I^\gamma$.

Table 5

Results for the Power Indices, the Dispersions, the Turbulent-to-Mean Magnetic Field Strength Ratios, the Line Widths, and the Mean Field Strengths

Region	Number of Pixels	γ^a	$s(\theta)$ (°)	b (°)	$\langle B_t^2 \rangle^{1/2}/B_0$	$\sigma_{(v)}$ (km s $^{-1}$)	B_0 (mG)
OMC-2/OMC-3	251	...	35.6	21.2 ± 0.8
OMC-3	116	-0.40 ± 0.01	27.1	12.1 ± 1.0
OMC-2	135	-0.66 ± 0.02	39.9	28.2 ± 0.8
MMS1 to MMS7	79	-0.38 ± 0.01	17.3	13.4 ± 0.9	0.17 ± 0.02	0.46^b	0.19
MMS8 to MMS10	37	-0.90 ± 0.04	11.9	11.1 ± 1.2	0.14 ± 0.02	...	$0.50 \times \sigma_{(v)}$
FIR1 and FIR2	42	-1.08 ± 0.05	35.6	22.9 ± 0.8	0.30 ± 0.02	...	$0.23 \times \sigma_{(v)}$
FIR3 to FIR5	36	-0.47 ± 0.04	34.9	26.0 ± 0.8	0.34 ± 0.02	0.65^c	0.13
FIR6 and south	57	-0.80 ± 0.05	39.7	33.8 ± 0.8	0.46 ± 0.02	...	$0.15 \times \sigma_{(v)}$

Notes.

^a Power indices obtained from plots similar to those shown in Figure 6.

^b Valid in OMC-3 MMS6, see Table 1 of Houde et al. (2000).

^c Valid in OMC-2 FIR4, see Table 1 of Houde et al. (2000).

We have calculated the power index γ for several subsets of the data shown in Figure 1. The division of the data into subsets was partially arbitrary but such that the number of pixels is still statistically significant for each subset. In each data set, the flux was normalized by its maximum flux value in the data set. Values of the power index are displayed in Column 3 of Table 5. The number of pixels used in the fit for each data set is given in Column 2 of the table. One can see strong variations of the power index from one region to the other. The region MMS1 to MMS7 is distinguished from the region MMS8 to MMS10 based on the fact that the polarization patterns have different mean orientations. Given the strong flux emission along certain lines of sight, the region of FIR1 and FIR2 was distinguished from the region of FIR3 to FIR5. The region of FIR6 was combined with the southernmost part of the map; these two areas contain a lot of pixels where no polarization was detected. This may introduce a bias in the estimation of the power index and one should be cautious in the interpretation of the results associated with these two areas.

3.3. CO Outflows and H₂ Jets

Williams et al. (2003) imaged CO outflows at 10'' resolution near several protostellar sources in OMC-2 and OMC-3. The outflow properties including their lengths are summarized in

their Table 1. We have used Figures 3–6 of their work to estimate the central coordinates and P.A.s of the molecular outflows spread along the filaments. Unbiased H₂ surveys for protostellar jets in Orion A were also conducted by Stanke et al. (1998, 2002). The positions, P.A.s, and lengths of the H₂ features are listed in Table 3 of Stanke et al. (2002). Since it was shown by Yu et al. (2000) that some of the jets cannot be associated with OMC-3 cores, only those associated with carbon monosulfide (CS) cores in OMC-3 (see Tatematsu et al. 1993; Aso et al. 2000) are considered in the following analysis.

All existing data associated with driving sources in OMC-2 and OMC-3 were used with the 850 μm data to produce a map where the polarization pattern is superimposed on jets and outflow P.A.s. Figure 7 shows such a map where CO outflows and H₂ jet lengths are appropriately scaled. CO outflows originating from MMS2/MMS3, MMS5, MMS7, MMS8, MMS9, MMS10, FIR1bc, FIR2, and FIR3 are shown as red lines and marked with a red full square symbol. This symbol shows the location of the Chini et al. (1997) dust condensations, but because many possible progenitors can be seen through FIR1bc and FIR2, they only indicate the geometrical centers of these flows. H₂ jets 4, 5, 14, 17, 18, 19, 21, 23, 24, and 25 (Stanke et al. 2002) associated with CS cores are shown with green lines and marked with a green full circle symbol, following the coordinates given in Columns 2 and 3 of Table 3 of Stanke

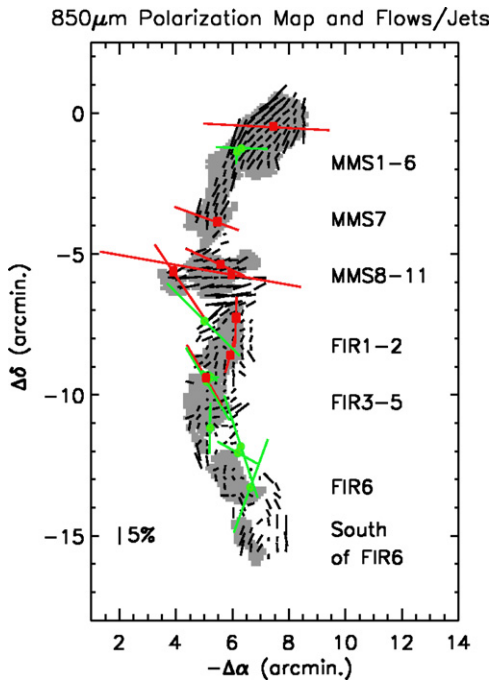


Figure 7. Distribution of H₂ jets (green) and CO outflows (red) superimposed on 850 μm polarization data (thin vectors). See Section 3.3 for explanations and Figure 1 for comparison with polarization vectors only. Some of the H₂ jets overplot CO outflows which make them difficult to see in the figure. Flow designations and coordinates are given with other information in Table 6. A background intensity map ($I(850 \mu\text{m}) \geq 0.5 \text{ Jy pixel}^{-1}$, where pixels are $3'' \times 3''$ in size) is displayed and shows the location of the filament. The reference position is R.A. = $5^{\text{h}}35^{\text{m}}48^{\text{s}}$, decl. = $-5^{\circ}00'0''$ (J2000.0).

(A color version of this figure is available in the online journal.)

et al. (2002). All of the H₂ jets included here are members of the “certain” group defined by Stanke et al. (2002) where flows are identified on morphological grounds. The coordinates are thus representative coordinates, meaning that if there is a candidate driving source, its position is given; alternatively, if the location of a possible driving source is suggested on morphological grounds like, for example, the geometric center of an apparently bipolar H₂ configuration, this position is given.

On this basis, a statistical study of the angular offsets on the POS between jet or outflow P.A.s and the P.A.s of the polarization vectors was carried out. The closest vectors on either side along the projected lengths were selected with the distance between polarization vectors and flows never being higher than $18''/6$; more typically, the distance was a few arcseconds. Each selected vector was used no more than one time. Each resulting mean angular offset is thus the difference between the P.A. of the outflow/jets and the mean of subsets of two to nine polarization P.A.s. Finally, we note that no jets are seen in the region south of FIR6 (Stanke et al. 2002) and that the CO observations of Williams et al. (2003) did not cover this region. A summary of our results is given in Table 6 where designations of the flows, the coordinates of the central source or of the central position, estimates of their P.A.s, estimates of the mean P.A.s of subsets of sub-mm vectors in their vicinity, and offsets between these P.A. estimates are displayed.

A histogram of the angular offsets between each polarization P.A. and jet/outflow orientation on the POS can be seen in Figure 8. A histogram of the mean angular offsets from Table 6 is also shown by a dashed line. With only 20 mean offset estimates, it is difficult to argue that the distribution is random rather

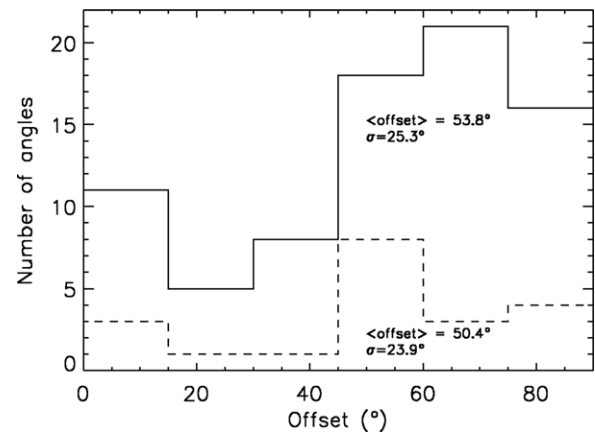


Figure 8. Solid line: distribution of angular offsets on the POS between H₂ jets and CO outflows P.A.s with 850 μm P.A.s of polarization vectors; see Figure 7. Dashed line: distribution of the mean angular offsets shown in Table 6. Details are given in Section 3.3.

Table 6
Jet/Outflow Versus Sub-mm Polarization Orientations

Flow ^a Designation	R.A. (J2000) (h m s)	Decl. (J2000) (° ' ")	P.A. _{flows} (°)	(P.A. _{sub-mm}) ^b (°)	ΔP.A. (°)
mms23	5 35 18.5	-5 00 28	87	-33	60
5/mms5	5 35 22.4	-5 01 16	90/88	-35	56
4	5 35 23.4	-5 01 31	-4	-28	24
mms7	5 35 26.5	-5 03 50	70	-17	87
mms8	5 35 26.5	-5 05 18	65	-63	52
mms9 ^(west)	5 35 26.0	-5 05 47	80	89	9
mms9 ^(east)	5 35 26.0	-5 05 47	80	-65	35
mms10	5 35 32.2	-5 05 47	34	-66	80
14	5 35 28.1	-5 07 20	45	-59	76
fir1bc	5 35 23.4	-5 07 48	-2	-53	51
fir2	5 35 24.5	-5 08 30	-15	-13	2
18	5 35 27.5	-5 09 17	56	-22	78
19	5 35 26.7	-5 09 24	-83	-28	55
17/fir3	5 35 27.5	-5 09 37	31	-57	72
21 ^(north)	5 35 27.2	-5 11 11	-1	-61	60
21 ^(south)	5 35 27.2	-5 11 11	-1	-3	2
23 ^(north)	5 35 22.8	-5 11 50	18	-58	76
23 ^(south)	5 35 22.8	-5 11 50	18	28	10
24	5 35 23.3	-5 12 03	61	-66	53
25	5 35 21.4	-5 13 14	-20	32	52

Notes.

^a Williams et al. (2003) used abbreviations fir and mss followed by numbers to identify CO outflows. Stanke et al. (2002) used single numbers to identify H₂ jets. We use their designations here.

^b Vectors lying at a distance less than $18''/6$ from the projected jet/outflow axis are used. No vector is used more than one time.

than normal. So to make a first test, the cumulative distribution function (CDF) of the 161 angular offsets is shown in Figure 9. The straight dotted line is the CDF expected for an infinite perfectly random sample. The distribution of the complete flow sample follows this line reasonably closely. With this sample we find that, statistically, the null hypothesis from a Kolmogorov test is accepted, meaning that the observed distribution is compatible with a random distribution and that the group of flows we compiled could be randomly oriented with respect to the polarization pattern of OMC-2 and OMC-3. Similarly, a χ^2 test applied to the observed distribution compared to the random distribution shows with great probability that these two distributions are similar.

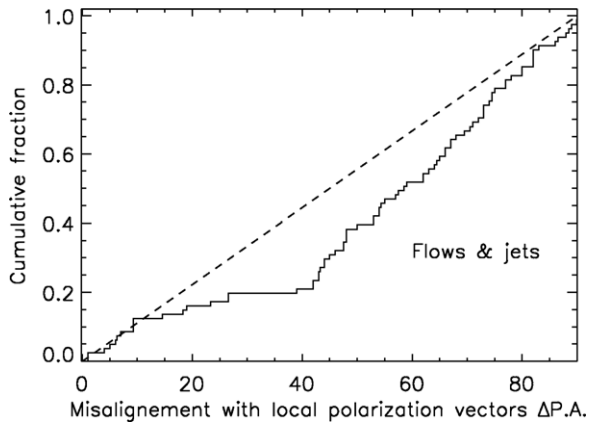


Figure 9. Cumulative distribution function of the difference in P.A.s between local sub-mm polarization vectors and jets/flows. The dashed line is the function expected for an infinite randomly oriented sample.

4. DISCUSSION

4.1. A Possible Impact of Jets and Outflows on Sub-mm Polarization Patterns

Based on the statistical tests presented in Section 3.3, we conclude that no correlation is evident between the relative orientation of jets or outflows and polarization vectors on the POS. This conclusion is similar to that of Ménard & Duchêne (2004) in the Taurus molecular cloud complex, an active star-forming region containing no massive stars. In their study, using absorption polarimetry data, these authors show that T Tauri stars as a group are apparently oriented randomly with respect to the local magnetic field. This indicates that even if the cloud’s magnetic field is dominant at large scale, its influence largely decreases on the much smaller scale of individual objects unless the orientation of these individual objects has changed since birth. The situation seems to be the same in the OMC-3/2 regions. This scenario also implies that if turbulence generated by the outflows is able to misalign grains in the envelopes of the cores, this effect cannot be seen on the POS with the resolution of the JCMT. For a distance $d \approx 414$ pc, this means that, independently of their orientation relative to the LOS, the energy injected by CO outflows and H_2 jets into the clouds appears not to have any impact on the polarization patterns which are observed with the presence of jets and outflows on scales of ≈ 7700 AU.

In addition, detections of polarized CO emission are now available. A good introduction about the subject and a summary of some results are given by Forbrich et al. (2008). Some detections were established by Girart et al. (1999) in NGC 1333 IRAS 4A (see also Girart et al. 2006), and by Greaves et al. (1999) toward the Galactic center and in the molecular clouds S140 and DR21. When the optical depth, τ , and the spatial distribution of the gas and of the magnetic fields are favorable, it is possible to detect CO polarization vectors perpendicular or parallel to the magnetic field (see Kylafis 1983). Except in the “2 pc ring” where the optical depth τ is relatively high, positive detections found in the other regions are consistent with orientations of magnetic fields inferred by sub-mm dust polarimetry. Thus, at the scales of their spatial resolution, these works suggest that the energy injected by jets and flows should have no substantial impact on the net polarization produced by dust grains aligned in the clouds. This appears to be consistent with the OMC-3 north region where the well-defined polarization pattern suggests that whatever the inclination angle relative to the LOS of the jets

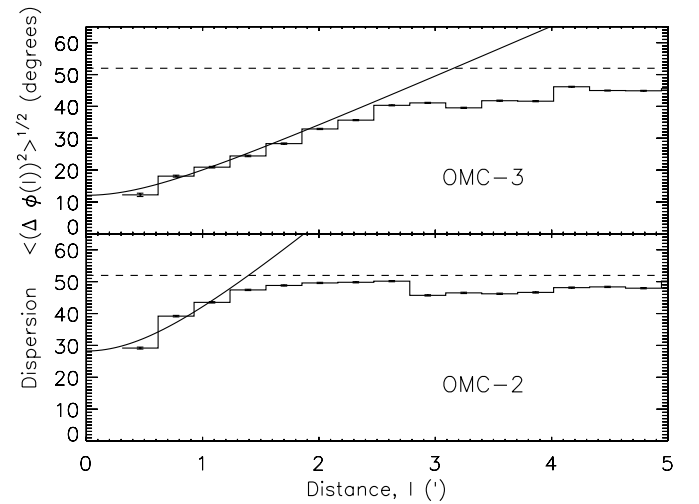


Figure 10. ADF, $\langle \Delta \Phi^2(l) \rangle^{1/2}$, for OMC-3 (top) and OMC-2 (bottom). The turbulent contribution to the total angular dispersion is determined by the zero intercept of the fit, b , to the data at $l = 0$ (see Table 5). The higher value of b for OMC-2 shows that it is more turbulent than OMC-3. The dashed line is the maximum dispersion that would be obtained in case of a purely random polarization angle distribution (Serkowski 1962).

and flows, as well as their orientation on the POS, the energy injection rate has no influence on the alignment of dust grains seen at the scale of the observations. In MMS7, the outflow is oriented perpendicular to the $850 \mu\text{m}$ polarization vectors covering this area. This means that if the situation is the same as in NGC 1333 IRAS 4A (Girart et al. 1999), polarized CO emission vectors should be seen perpendicular to these vectors. In MMS8, 9, and 10, the analysis of the situation is different since in this part of the sky the polarization pattern orientation may be due to another superimposed crossing filament or by a bend of the filament (see Matthews et al. 2001). Since the association of jets and outflows with their probable progenitors is not always certain because of overlapping effects on the sky, a better understanding of the magnetic field structure producing the sub-mm polarization pattern observed in the southern part of OMC-3 and in the northern part of OMC-2 added to polarized CO emission observations could help to constrain these associations.

The analysis of the situation in OMC-2 is not exactly the same since some of the high intensity regions are devoid of detections. However, in regions where polarization vectors have an S/N such that $p/\sigma_p > 3$ the general conclusion about the relative orientation of the jets/outflows with the sub-mm polarization vectors discussed above is still valid.

4.2. Turbulent Angular Dispersions

The second-order structure function of the polarization angles is defined as the average of the squared difference between the polarization angle measured at two points separated by a distance l (see Equation (5) given by Falseta-Gonçalves et al. 2008). Once applied to a grid of pixels containing polarization P.A. information, a fit to the square root of this function, namely, the angular dispersion function (ADF), gives a method for estimating the turbulent contribution to the total angular dispersion. First applications of the method and results obtained in regions OMC-1, DR21 Main, and M17 are given by Hildebrand et al. (2009).

Figure 10 shows the ADF obtained after application of the method on the $18''6$ square pixel grid to the maps of OMC-3 and

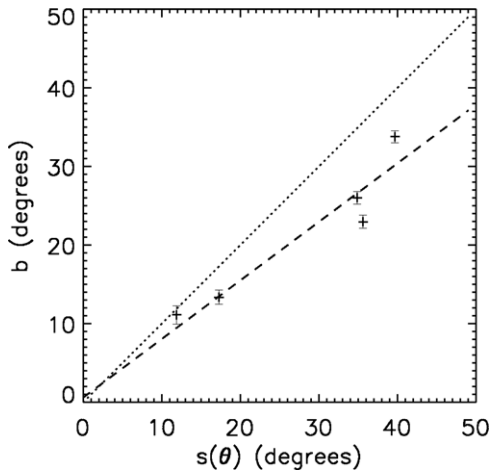


Figure 11. Turbulent dispersion component, b , estimated with ADF, $(\Delta\Phi^2(l))^{1/2}$, vs. dispersion of polarization angles, $s(\theta)$, for regions displayed in Table 5. The dotted line expresses equality between these two quantities. The linear fit applied to the data and shown by the dashed line gives the relation $b = (0.60 \pm 1.24) \text{ deg} + (0.75 \pm 0.04) \times s(\theta)$.

OMC-2 shown in Figure 1. The dashed line shows the maximum dispersion value, $b_{\max} = \frac{180^\circ}{\sqrt{12}}$, that would be reached in the case of a purely random polarization angle distribution (see Serkowski 1962). All the maps obtained in several regions of the filament are not shown here but the turbulent angular dispersion fitting parameter, b , was estimated for each region displayed in Table 5. Estimates of b obtained with the correlation method for OMC-2/OMC-3, OMC-3, OMC-2, and the five subregions selected along the filament (see discussion in Section 3.2) are displayed in Column 5 of Table 5. These values can be compared to the angular dispersion values, $s(\theta)$ obtained with the square root of the variance of the data sets displayed in Column 4 of the table. Figure 11 shows the variation of b with $s(\theta)$ for the five subregions. The dotted line expresses equality between these two quantities. A linear fit applied to the data and shown by the dashed line returns the relation, $b = (0.60 \pm 1.24) \text{ deg} + (0.75 \pm 0.04) \times s(\theta)$, meaning that the angular dispersion values estimated with the correlation method are statistically about 25% lower than the ones calculated about the mean polarization P.A.

The ratio of turbulent to large scale magnetic field is estimated by using Equation (7) given by Hildebrand et al. (2009)

$$\frac{\langle B_t^2 \rangle^{1/2}}{B_0} = \frac{b}{\sqrt{2 - b^2}} \quad (6)$$

and values are displayed in Column 6 of Table 5. In cases where the turbulent component of the field is very small compared to the nonturbulent component, $B_t \ll B_0$, Hildebrand et al. (2009) show that the uniform component of the field can be approximated by the following equation:

$$B_0 \simeq \sqrt{8\pi\rho} \frac{\sigma_v}{b}. \quad (7)$$

We use this approach by assuming a density of 10^4 cm^{-3} and a mean molecular weight of 2.3. Estimates of B_0 are given as a function of σ_v in the last column of Table 5 except for regions MMS1 to MMS7 and FIR3 to FIR5 since line width measurements from $\text{H}^{13}\text{CO}^+ J = 3 \rightarrow 2$ were made in OMC-3 MMS6 and OMC-2 FIR4 by Houde et al. (2000). We use the values shown in their Table 1 to directly make estimates

of B_0 . The line width measurements are reported in Column 7 of Table 5. Given the smooth and well-defined polarization patterns observed in regions MMS1 to MMS7 and MMS8 to MMS10, we are confident that the method is suitable to estimate, within a factor of a few, the global mean field component. In the three other subregions, the higher dispersion polarization patterns suggest that the relation $B_t \ll B_0$ may not be as well satisfied. However, all in all, the results shown in Table 5 are a first step to intercompare the regions.

The estimates of the turbulent angular dispersion components, b , displayed in Column 5 of Table 5 for OMC-3 and OMC-2 are all higher than those estimated by Hildebrand et al. (2009) in their Table 1. We point out that the turbulent component dispersion estimates obtained in OMC-3 are of the same order than those found in regions OMC-1 and M17. On the contrary, the high value obtained in OMC-2 distinguishes this region from OMC-3, OMC-1, M17, and DR21 (Main). Hildebrand et al. (2009) find that the dispersions obtained about the mean field orientation are about a factor of 3 times higher than the ones estimated by using the ADF fitting method. Doing the same comparisons, we find a factor of about 2–1.5 for regions OMC-3/OMC-2, OMC-2, and OMC-3.

Abundances of molecular species and clumping studied by Batrla et al. (1983), Castets & Langer (1995), and Chini et al. (1997) suggest an evolutionary effect from north to south along OMC-2/3. The two regions could have different ages and OMC-3 could be younger than OMC-2. This could explain why OMC-2 and OMC-3 are so different from the point of view of sub-mm polarization data. On the other hand, the situation is not so clear since Takahashi et al. (2008) show that some IM objects can be at a more evolved stage in OMC-3 than in OMC-2. Another explanation could invoke some effects of the radiation field. Since OMC-3 is at a higher distance to OMC-1 than OMC-2 is, the local ISRF dominated by the bright stars located in the nebulae in front of OMC-1 could be more efficient to shape the OMC-2 region than the OMC-3 region. The two regions, OMC-2 and OMC-3, could have the same age but the erosion produced by the local ISRF could be stronger on OMC-2 than on OMC-3.

4.3. Ordered Versus Turbulent Magnetic Field Components Along OMC-2 and OMC-3

4.3.1. Depolarization and Turbulence Along the Filaments

Table 5 suggests that depolarization is present toward the OMC-2 sources as much as toward OMC-3. To understand how the decrease of polarization with the increase of intensity could be related to turbulent arguments, we show in Figure 12 the variations of the power indices of the p – I relation, γ , with the turbulent angular dispersion components, b , for the five subregions in Table 5. We find no specific correlation, meaning that the decrease of the polarization degree observed appears independent of turbulent flows or turbulent effects that could be present into the densest regions of the cloud. On the other hand, the variation of the mean polarization degrees, $\langle p \rangle$, with the turbulent angular dispersion estimates, b , of the regions considered in Table 5 and shown in Figure 13 suggests an anti-correlation between the two parameters. If this trend is real, it would mean that, independently of the ordered magnetic field structure component, the mean polarization degree observed in a given region could be a function of the turbulent magnetic field component. To test this hypothesis, we did a linear fit of the form $\langle p \rangle = \langle p_0 \rangle + c_1 \times b$, to the eight points displayed

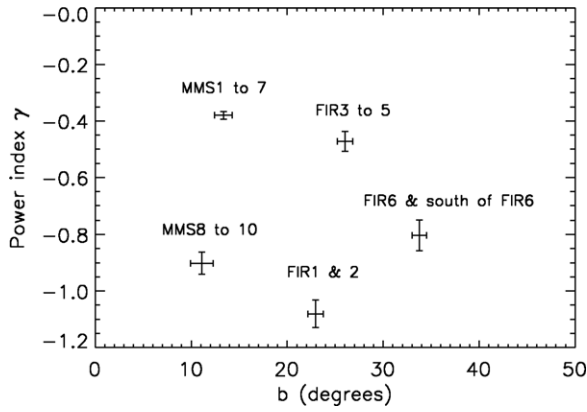


Figure 12. Distribution of, b , fitting parameter of the turbulent dispersion component estimated with ADF, $\langle \Delta\Phi^2(t) \rangle^{1/2}$, vs., γ , power index translating the decrease of p with normalized fluxes (see Figure 6) for regions displayed in Table 5.

in Figure 13. The results are $\langle p_0 \rangle = 4.2\% \pm 0.2\%$ and $c_1 = -0.07\% \text{ deg}^{-1} \pm 0.01\% \text{ deg}^{-1}$, where the fit is constrained by taking into account the errors on p . The errors are estimated by dividing the standard deviation of each data set by the square root of the number of data. In addition, a fit of the variations of b with $\langle p \rangle$ (not shown here) of the form $b = b_0 + c_2 \times \langle p \rangle$, taking into account the uncertainties on b , gives the results $b_0 = 54.2 \pm 1.5$ and $c_2 = -11.8 \text{ deg}\%^{-1} \pm 0.6 \text{ deg}\%^{-1}$. Given the errors on p , the first fit constrains reasonably the variations of $\langle p \rangle$ with b . Within the uncertainties the intersect of the fit with the abscissa axis gives a value of b_0 which is hardly consistent with the expected value, b_{max} of about 52° , that would be found in the case of a purely random polarization P.A. distribution (Serkowski 1962). On the contrary, the second fit returns a value b_0 relatively close to that of b_{max} suggesting that if such a region was observable the mean polarization degree could be about zero.

To test if the trend observed in OMC-2/OMC-3 is consistent with the polarization properties of OMC-1, we use the turbulent dispersion parameters, b , estimated by Hildebrand et al. (2009) in their Table 1 and Figure 3 of Vaillancourt et al. (2008) where median polarization ratios are displayed for different wavelengths and for several regions. The mean polarization percentage observed at $350 \mu\text{m}$ by Houde et al. (2004) is $\langle p \rangle = 2.7\%$ with a dispersion $\sigma_p = 1.4\%$. Using Figure 3 shown by Vaillancourt et al. (2008) and a wavelength ratio of 1.3, a mean polarization of about 3.5% should be representative of the mean degree of polarization observed at $850 \mu\text{m}$ in OMC-1 with $12''$ resolution. Neglecting the effects that could produce a slightly lower resolution of $14''$ and with the assumption that the turbulent ratios derived with $350 \mu\text{m}$ and $850 \mu\text{m}$ polarization maps would be similar this yields a point ($b = 8.3 \pm 0.3$, $\langle p \rangle \approx 3.5\%$) that appears to be consistent with our fit.

A similar trend was observed along the Pipe Nebula by Alves et al. (2008) with R -band visible polarization data collected for about 12,000 stars. In this case, the dispersion of several subsets of polarization P.A.s is used to estimate the turbulence of regions having a mean density $n(\text{H}_2) \approx 10^3 \text{ cm}^{-3}$ and is compared to the mean polarization degrees of the subsets of data. The regions probed in the Pipe Nebula have densities about an order of magnitude lower than the density considered in our calculations where sub-mm data would mostly probe the inner fields embedded in the filaments.

The estimates of the mean field strength displayed in Table 5 for regions MMS1 to MMS7 and FIR3 to FIR5 are of the same

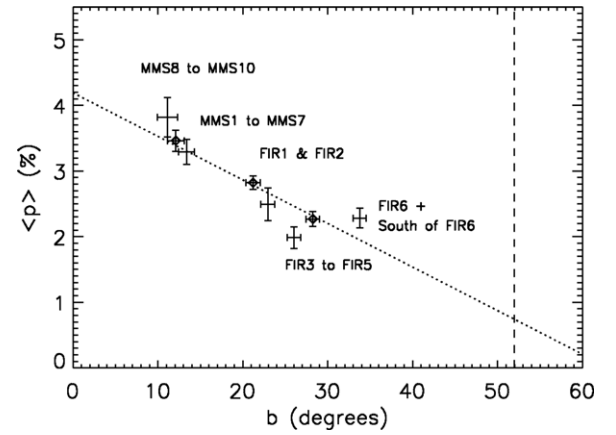


Figure 13. Distribution of, $\langle p \rangle$, mean polarization degree for the regions displayed in Table 5, vs., b , fitting parameter and turbulent dispersion component estimated with the angular dispersion function, $\langle \Delta\Phi^2(t) \rangle^{1/2}$. Regions OMC-2/OMC-3, OMC-3, and OMC-2 are shown with diamonds. The errors on the mean polarization values are shown as vertical error bars. The fit discussed in Section 4.3.1 is shown by the dotted line. The vertical dashed line displays the maximum turbulent component of about 52° theoretically reachable.

order. This result dismisses the hypothesis that the dust grain alignment efficiency could decrease with the magnetic field strength. In addition, mean inclination angles of the magnetic field from the LOS were estimated by Houde et al. (2004) to vary from about 73° to about 80° in three dense regions displayed along OMC-2/OMC-3. If these inclination angles are representative of the mean inclination angle of the magnetic field along the filaments and if the grains are aligned with roughly the same efficiency everywhere then the degree of polarization would not be very sensitive to this parameter. These two points do not dismiss the possibility that the mean polarization degree of some regions could be a function of the level of turbulence in the region, but they also do not rule out the possibility of complex structures of an ordered magnetic field component. In cases where the large scale magnetic field dominates over the turbulence it could be that some superposition effects along the LOSs would produce a decrease of the polarization degree with an increase of the polarization P.A. dispersion over some regions. These aspects are discussed in the following sections.

4.3.2. Effects of Steady-state Magnetic Field Models

The turbulent-to-mean magnetic field strengths ratios displayed in Table 5 imply intensities of the turbulent magnetic component about six to seven times lower than the mean magnetic field component into the OMC-3 filaments. This ratio supports the steady-state magnetic field approach proposed by Fiege & Pudritz (2000) and applied to the OMC-3 region as discussed by Matthews et al. (2001). In the work of Fiege & Pudritz (2000), the maximum polarization degree is calibrated with sub-mm observations and dust grains are aligned perpendicular to the magnetic fields. The combination of toroidal with poloidal magnetic fields components leads to superposition effects along the same LOS. This geometrical effect decreases the net polarization on the POS and renders uniform magnetic fields indistinguishable from a helical field geometry. The model can reproduce the r^{-2} density profile⁴ observed by Johnstone & Bally (1999) and could explain the depolarization observed along the spine of the filament. A similar approach was followed by Gonçalves et al. (2005) with a focus on molecular cloud cores and shows

⁴ Here, r is the radial distance, in cylindrical coordinates.

that tangling of the magnetic field orientations by the effects of gravity could produce polarization maps showing an significant angular dispersion from the mean uniform field. Since it is not clear that OMC-2 is a clear case of a magnetically dominated region with respect to the turbulence, it would be interesting to test under which conditions steady-state magnetic models could reproduce the polarization properties observed in this region.

4.3.3. Variation of MHD Models

The statistical results shown in Figure 13 discussed above in Section 4.3.1 suggest that turbulence could be a parameter regulating the mean degree of polarization observed in a given polarization map. One open question would be to understand to what extent magnetohydrodynamic (MHD) models could reproduce such a decrease of polarization.

Falceta-Gonçalves et al. (2008) present results for turbulent, isothermal, three-dimensional simulations of sub/supersonic and sub/super-Alfvénic cases. Dust grains are assumed perfectly aligned and perpendicular to the magnetic field. Depolarization is due to the dispersion increase of the polarization P.A.s and is a function of the MHD regime considered as well as of the orientation of the initial uniform magnetic field with respect to the LOS. The dust total intensity is assumed to be proportional to the column density. The high resolution of the simulations provides less homogeneous magnetic field structures and higher density contrasts than previous models.

On the other hand, Cho & Lazarian (2005) show that under peculiar conditions depolarization could occur if grains embedded in dark clouds are aligned by radiative torques (RATs) such that their long axis is perpendicular to the magnetic field. In their model, the nonturbulent field is about two times stronger than the fluctuating magnetic field, a condition encountered in OMC-2 (see Table 5) and the ordered component is assumed to be uniform and in the POS. This condition may exist along the length of the OMC-2 and OMC-3 filaments (Houde et al. 2004). Additionally, the results proposed by Cho & Lazarian (2005) are valid for clouds without embedded massive stars, a condition valid in OMC-2/3 where forming stars are of intermediate (see Takahashi et al. 2008) or lower mass. Two interesting extensions to the Cho & Lazarian (2005) work were proposed by Pelkonen et al. (2007) and by Bethell et al. (2007) but the analysis of the simulations is focused on the effects of RATs on depolarization rather than on the effects of the turbulent regimes on depolarization. Alignment by RATs is not considered by Falceta-Gonçalves et al. (2008) but an anti-correlation between the polarization degree and the column density, with exponent $\gamma \sim -0.5$ is predicted, due to random cancellation of polarization vectors along the LOS. This value is close to some values obtained on larger scales in OMC-2 and OMC-3 under conditions which are discussed in more detail in the following section. Comparisons done by Falceta-Gonçalves et al. (2008) between four different MHD regimes show a degeneracy between the Alfvénic Mach number and the angle between the mean magnetic field and the LOS. They discuss the effects of different resolutions on the structure function of the polarization angle and the applicability of these structure functions to the determination of turbulent cutoff scales.

A comparison of the 14'' resolution 850 μm P.A. histogram displayed in Figure 4 with the results of Figure 4 of Falceta-Gonçalves et al. (2008) would reject the presence of super-Alfvénic modes in OMC-3 and probably in OMC-2 as well. This inference would be consistent with the lack of correlation between jets/outflows and polarization vectors discussed in

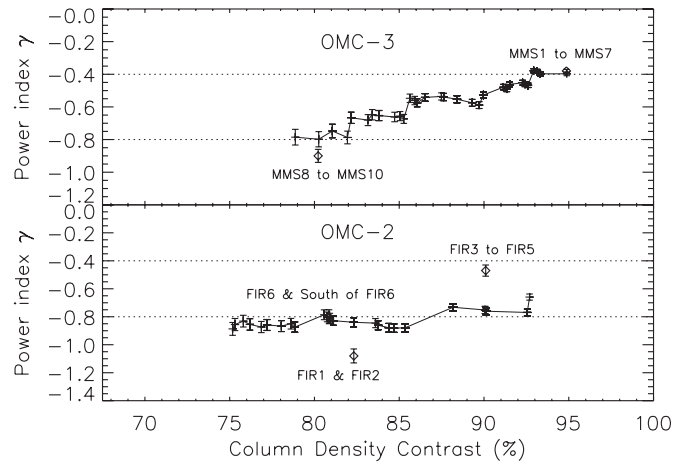


Figure 14. Distribution of the power index of the p - I relation with the column density contrast, $\text{CDC} = (\text{Flux}_{\text{max}} - \text{Flux}_{\text{min}})/\text{Flux}_{\text{max}}$. Diamonds show the CDC and power index values for the subregions identified in Table 5, without masking any values. The solid lines trace the behavior of the power index as the CDC varies with each subsequent masking of high intensity pixels (for a full explanation, see the text). The OMC-3 region is shown in the top panel and the OMC-2 region in the bottom panel. The horizontal dashed lines show the two regimes discussed in Section 4.3.4.

Section 4.1. But, as suggested in other regions by Padoan et al. (2004), this would not rule out the presence of super-Alfvénic modes at smaller scale, in cores of about 0.25 pc in size in the OMC-2/3 regions for a distance to the clouds of about $d = 414$ pc (see Menten et al. 2007). Finally, because of the resolution of our data, a direct comparison of our results with the structure function of the polarization P.A. calculated for different MHD regimes is not done.

4.3.4. Variations of Power Index with Column Density Structure

Figure 13 illustrates that the mean polarization degree of any region could be controlled by the MHD regime but it does not give any indication about the possible effect of the MHD regime on the level of depolarization. Figure 12 shows an absence of correlation between the power index of the p - I relation and the turbulence parameter, b , however, and suggests that one or more phenomena other than turbulence should be considered. To inform this discussion, we consider possible variations in column density structure and the power-law index, our best quantifier of depolarization.

Estimates of the power indices of the five subregions from Table 5 are shown as a function of the column density contrast, $\text{CDC} = (\text{Flux}_{\text{max}} - \text{Flux}_{\text{min}})/\text{Flux}_{\text{max}}$, in Figure 14. On a statistical basis, the variation of the power index with the CDC is estimated by considering the several maps obtained by masking high intensity pixels above specific cutoffs. These variations of the power indices with the CDCs are shown by the solid lines in Figure 14. The highest CDC values are derived from our original maps (Figure 1). To establish the power index of lower column material, for which we assume lower fluxes to be a proxy, we methodically masked the highest pixels by using a step of 33 mJy/18''6 in column density and then recalculated the CDC and power index of the resulting p - I relation. By repeating this process, we are able to assess the impact of lower and lower column material on γ . We stopped at the level of 26% of the peak in OMC-3 (71 of 116 pixels were used in the process) and 30% of the peak in OMC-2 (108 of 135 pixels). Below these values, divergences were observed in the estimates of γ , likely due to the small sampling statistics.

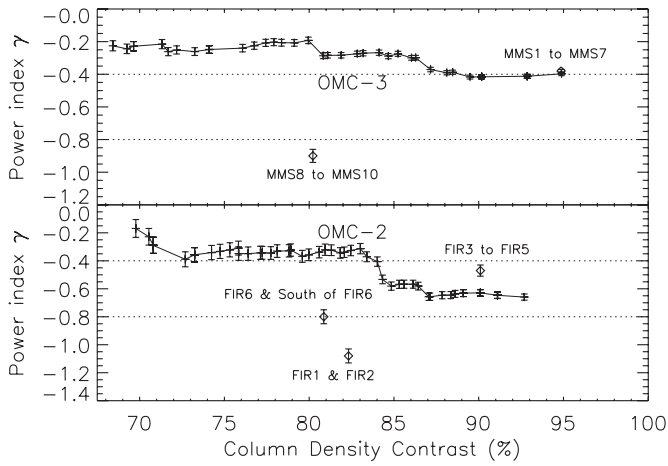


Figure 15. Same as Figure 14, but instead of high intensity pixel masking, low intensity pixels are progressively masked out.

In OMC-3, the power index shows almost a linear decrease from $\gamma = -0.8$ down to $\gamma = -0.4$. The upper value suggests a first regime reflecting the statistical level of depolarization obtained when the cores and the high density flux regions are included and well represented. The lower value suggests another regime corresponding to the statistical level of depolarization obtained when the high density flux regions are avoided. Along OMC-2, only a small range of variation is observed with $\gamma \approx -0.8$, perhaps reflecting the fact that polarization was not detected in many of the brightest regions. The two regimes are illustrated by the two horizontal dashed lines shown in Figure 14.

To test the possibility of two regimes, we applied the same process in reverse, preferentially masking the lowest flux pixels until reaching 31% of the peak in OMC-3 (31 of 116 pixels were used in the process) and 30% of the peak in OMC-2 (25 of 135 pixels). The subsequent variations of the power index of the p - I relation with the CDC are plotted on Figure 15. Here again the effect of the cores seems to be under represented on larger scale in OMC-2 and the power index is constant and about -0.6 in the density contrast range $\text{CDC} \approx 84\%$ – 93% . Once the lowest density structures are avoided, however, a second regime appears and the power index is constant and about -0.4 in the density contrast range $\text{CDC} \approx 73\%$ – 84% . In OMC-3, the power index is constant and about -0.4 in the density contrast range $\text{CDC} \approx 87\%$ – 95% . Below a $\text{CDC} \approx 87\%$, the power index increases from about -0.4 to -0.2 , showing the effects a reduction of the coverage mapping centered around high density regions could produce.

Finally, when comparisons are done between the five subregions, the effect of the presence of the cores on the measured power index is clearer. The two regions FIR3 to FIR5 and MMS1 to MMS7 are consistent with the first regime where the cores are included since the maximum intensity pixel used to normalize the intensity of the p - I relation are the same as those used in OMC-2 and OMC-3, respectively. Interestingly, the relatively low density region FIR6 and south of FIR6 appears consistent with the second regime where the effects of the cores are avoided. Departures from the two regimes are observed in the MMS8 to MMS10 and particularly FIR1 and FIR2 regions. The maximum intensity pixels used to normalize the intensity of the p - I relation are small in these regions compared to the one used in region FIR6 and south to FIR6. This makes the sizes of the samples of regions MMS8 to MMS10 and FIR1 and FIR2 too small to be representative of the density struc-

ture of one of the two apparent regimes observed on larger scale.

In conclusion, if representative of the column density structure of the molecular cloud, the presence of cores can lead to two distinct regimes of depolarization: one with a shallower power index reflecting the cores and a steeper value representative of lower column density material. We note, as pointed out in observational works (see Anderson et al. 2007; Whittet et al. 2008), that dust alignment by RATs could be a promising ingredient for understanding depolarization. In this framework, a possible explanation for the shallower power index in cores could be the growth of larger, non-spherical grains in dense, cold condensations. As a consequence, the upper cutoff of the power-law distribution of grain sizes will be higher in maps including cores than without cores and the power index of the p - I relation be lower (see Figure 6 in the work of Cho & Lazarian 2005). An alternative explanation could be an enhancement of gravity high enough to distort the magnetic field orientations in the cores. This mechanism will tend to decrease the net polarization and the values of the power index will change accordingly (see Gonçalves et al. 2005 and details given in Section 4.3.2). We note that our analysis could be subject to a bias if the resolution of the instrument is too small to properly sample the column density structure of the clouds. Because the Williams et al. (2003) interferometric mapping in OMC-2/3 precludes any multi-core scenario, the analysis of our data should not be subject to a bias due to intercept of cores along the same LOS, a possibility discussed by Pelkonen et al. (2007).

5. SUMMARY

Eight hundred fifty micron SCUBA polarization data of OMC-2 were homogeneously reduced in combination with archived data of OMC-3. Our main results are as follows.

1. In OMC-2, the polarization pattern shows more variations of polarization P.A.s on spatial scales similar to those of the two well-ordered polarization patterns observed in OMC-3. The mean degree of polarization is lower in OMC-2 than in OMC-3. We find that vectors in FIR1 suggest a realignment of the polarization vectors with the filament in the region south of OMC-3.
2. In regions of existing $350 \mu\text{m}$ polarization data, we find that except in FIR6, $850 \mu\text{m}$ polarization vector patterns are similar to those at $350 \mu\text{m}$. Significant detections are only available at $850 \mu\text{m}$ in and around three regions, namely: MMS7, FIR1 and FIR2, and in the region south of FIR6.
3. A comparison of the offsets between P.A.s of CO outflows/ H_2 jets and polarization vectors suggests that no specific orientation of these outflows relative to the polarization patterns can be found. This fact suggests that if dust grains are generally aligned with their long axis perpendicular to the magnetic field, there is no correlation between outflows and the mean magnetic field orientation on the POS, at least to the $14''$ beam resolution of our data.
4. Based on the hypothesis that turbulence is present along the filaments, second-order structure functions of the polarization P.A. show that OMC-3 is a less turbulent region than OMC-2. OMC-3 appears to be a clear case of a magnetically dominated region with respect to the turbulence. However, for OMC-2, it is not clear that this is the case. In OMC-2 and OMC-3, the dispersions obtained about the mean field orientation are factors of 1.5–2 times higher than those estimated with the angular dispersion fitting method.

Estimates of the projected magnetic field strengths associated with the objects MMS6 and FIR4 are calculated to be 0.19 mG and 0.13 mG, respectively.

5. A more in-depth analysis provides estimates of the power index, γ , also known as the depolarization parameter, the dispersions obtained about the mean field orientation $s(\theta)$ and with the angular dispersion fitting method b , the turbulent-to-mean magnetic field strength ratio $\langle B_t^2 \rangle^{1/2} / B_0$ for five regions along OMC-3 and OMC-2. We find an anti-correlation between $\langle p \rangle$, the mean polarization degree, and the turbulence parameter b , meaning that the level of turbulence in a region could regulate the mean polarization degree observed. No specific correlation is found between γ and the turbulence parameter b .
6. When steady-state models are considered, two scenarios can explain the polarization at the southern edge of OMC-3: a bent filament and a second filament oriented almost orthogonal to the ISF (see Matthews et al. 2001). How the relative effects of steady-state and turbulent magnetic field models contribute to the observed polarization in OMC-2 have yet to be quantified.
7. If the mapping sufficiently reflects the column density structure of the clouds, a statistical analysis suggests the presence of two depolarization regimes in our maps. One regime including the effects of the cores, the other one excluding it.

The authors thank G. Schieven at the JCMT for his assistance during and after observing, R. L. Curran at the Dublin Institute for Advanced Studies for her help during the data reduction process, and an anonymous referee for useful suggestions. F.P.'s research was supported by the Conseil de Recherche en Sciences Naturelles et en Génie du Canada. This author also thanks the Fundação de Amparo à Pesquisa do Estado de São Paulo (FAPESP grant number 2007/56302-4) for support during the second phase of the present research. P.B.'s research is supported by the Conseil de Recherche en Sciences Naturelles et en Génie du Canada. B.M.'s research is supported by a Plaskett Fellowship at the National Research Council of Canada.

REFERENCES

- Aitken, D. K., Smith, C. H., Moore, T. J. T., Roche, P. F., Fujiyoshi, T., & Wright, C. M. 1997, *MNRAS*, **286**, 85
- Alves, F. O., Franco, G. A. P., & Girart, J. M. 2008, *A&A*, **486**, L13
- Andersson, B. G., & Potter, S. B. 2007, *ApJ*, **665**, 369
- Aso, Y., Tatematsu, K., Sekimoto, Y., Nakano, T., Umemoto, T., Koyama, K., & Yamamoto, S. 2000, *ApJS*, **131**, 465
- Batrla, W., Wilson, T. L., Bastien, P., & Ruf, K. 1983, *A&A*, **128**, 279
- Bethell, T. J., Chepurinov, A., Lazarian, A., & Kim, J. 2007, *ApJ*, **663**, 1055
- Castets, A., & Langer, W. D. 1995, *A&A*, **294**, 835
- Chini, R., Reipurth, B., Ward-Thompson, D., Bally, J., Nyman, L.-Å., Sievers, A., & Billawala, Y. 1997, *ApJ*, **474**, L135
- Cho, J., & Lazarian, A. 2005, *ApJ*, **631**, 361
- Coppin, K. E. K., Greaves, J. S., Jenness, T., & Holland, W. S. 2000, *A&A*, **356**, 1031
- Di Francesco, J., Johnstone, D., Kirk, H., MacKenzie, T., & Ledwosinska, E. 2008, *ApJS*, **175**, 277
- Dotson, J. L., Davidson, J., Dowell, C. D., Schleuning, D. A., & Hildebrand, R. H. 2000, *ApJS*, **128**, 335
- Falceta-Gonçalves, D., Lazarian, A., & Kowal, G. 2008, *ApJ*, **679**, 537
- Fiege, J. D., & Pudritz, R. E. 2000, *ApJ*, **544**, 830
- Forbrich, J., Wiesemeyer, H., Thum, C., Belloche, A., & Menten, K. M. 2008, *A&A*, **492**, 757
- Girart, J. M., Crutcher, R. M., & Ramprasad, R. 1999, *ApJ*, **525**, L109
- Girart, J. M., Rao, R., & Marrone, D. P. 2006, *Science*, **313**, 812
- Gonçalves, J., Galli, D., & Walmsley, M. 2005, *A&A*, **430**, 979
- Greaves, J. S., Holland, W. S., Friberg, P., & Dent, W. R. F. 1999, *ApJ*, **512**, L139
- Greaves, J. S., et al. 2003, *MNRAS*, **340**, 353
- Hildebrand, R. H., Dotson, J. L., Dowell, C. D., Schleuning, D. A., & Vaillancourt, J. E. 1999, *ApJ*, **516**, 834
- Hildebrand, R. H., Dragovan, M., & Novak, G. 1984, *ApJ*, **284**, L51
- Hildebrand, R. H., Kirby, L., Dotson, J. L., Houde, M., & Vaillancourt, J. 2009, *ApJ*, **696**, 567
- Holland, W., Wayne, S., & Cunningham, C. R. 1998, *Proc. SPIE*, **3357**, 305
- Houde, M., Dowell, C. D., Hildebrand, R. H., Dotson, J. L., Vaillancourt, J. E., Phillips, T. G., Peng, R., & Bastien, P. 2004, *ApJ*, **604**, 717
- Houde, M., Peng, R., Phillips, T. G., Bastien, P., & Yoshida, H. 2000, *ApJ*, **537**, 245
- Jenness, R., Lighfoot, J. F., & Holland, W. S. 1998, *Proc. SPIE*, **3357**, 548
- Johnstone, D., & Bally, J. 1999, *ApJ*, **510**, L49
- Keene, J., Hildebrand, R. H., & Whitcomb, S. E. 1982, *ApJ*, **252**, L11
- Kylafis, N. D. 1983, *ApJ*, **267**, 137
- Lazarian, A. 2003, *J. Quant. Spectrosc. Radiat. Transfer*, **79**, 881
- Lazarian, A. 2007, *J. Quant. Spectrosc. Radiat. Transfer*, **106**, 225
- Lis, D. C., Keene, J., Dowell, C. D., Benford, D. J., Phillips, T. G., Hunter, T. R., & Wang, N. 1998, *ApJ*, **509**, 299
- Matthews, B. C., Lai, S.-P., Crutcher, R. M., & Wilson, C. D. 2005, *ApJ*, **626**, 959
- Matthews, B. C., McPhee, C., Fissel, L., & Curran, R. L. 2009, *ApJS*, **182**, 143
- Matthews, B. C., & Wilson, C. D. 2000, *ApJ*, **531**, 868
- Matthews, B. C., Wilson, C. D., & Fiege, J. D. 2001, *ApJ*, **562**, 400
- Ménard, F., & Duchêne, G. 2004, *A&A*, **425**, 973
- Menten, K. M., Reid, M. J., Forbrich, J., & Brunthaler, A. 2007, *A&A*, **474**, 515
- Padoan, P., Jimenez, R., Juvela, M., & Nordlund, Å. 2004, *ApJ*, **604**, L49
- Park, G., & Choi, M. 2006, *J. Korean Astron. Soc.*, **39**, 31
- Pelkonen, V.-M., Juvela, M., & Padoan, P. 2007, *A&A*, **461**, 551
- Rao, R., Crutcher, R. M., Plambeck, R. L., & Wright, M. C. H. 1998, *ApJ*, **502**, L75
- Schleuning, D. A. 1998, *ApJ*, **493**, 811
- Serkowski, K. 1962, *Adv. Astron. Astrophys.*, **1**, 289
- Stanke, T., McCaughrean, M. J., & Zinnecker, H. 1998, *A&A*, **332**, 307
- Stanke, T., McCaughrean, M. J., & Zinnecker, H. 2002, *A&A*, **392**, 239
- Takahashi, S., Saito, M., Takakuwa, S., & Kawabe, R. 2008, *Ap&SS*, **313**, 165
- Tatematsu, K., et al. 1993, *ApJ*, **404**, 643
- Vaillancourt, J. E., et al. 2008, *ApJ*, **679**, L25
- Vallée, J., & Bastien, P. 1999, *ApJ*, **526**, 819
- Vallée, J., & Fiege, J. 2007, *AJ*, **133**, 1012
- Whittet, D. C., Hough, J. H., Lazarian, A., & Hoang, T. 2008, *ApJ*, **674**, 304
- Williams, J. P., Plambeck, R. L., & Heyer, M. H. 2003, *ApJ*, **591**, 1025
- Yu, K. C., Billawala, Y., Smith, M. D., Bally, J., & Butner, H. M. 2000, *AJ*, **120**, 1974